Synthesis and characterization of $^{11}B_4C$ containing Ni/Ti multilayers using combined neutron and X-ray reflectometry

Sjoerd Broekhuijsen,[1] Naureen Ghafoor,[1] Alexei Vorobiev,[2,3] Jens Birch,[1] Fredrik Eriksson[1,*]

[1]*Department of Physics, Chemistry, and Biology, IFM, Linköping University, SE-581 83 Linköping, Sweden*
[2]*Department of Physics and Astronomy, Material Physics, Uppsala University, SE-751 20 Uppsala, Sweden*
[3]*Institut Max von Laue—Paul Langevin, 71 avenue des Martyrs, 38000 Grenoble, France*
[*]fredrik.eriksson@liu.se

Abstract

The performance of multilayers in optical components such as used in neutron scattering instruments is crucially dependent on the achievable interface width. We have shown how the interface width of Ni/Ti multilayers can be improved using the incorporation of B_4C to inhibit the formation of nanocrystals and limit interdiffusion and intermetallic reactions at the interfaces. A modulated ion-assistance scheme was used to prevent intermixing and roughness accumulation throughout the layer stack. In this work we investigate the incorporation of low-neutron-absorbing $^{11}B_4C$ for Ni/Ti neutron multilayers. Combined fitting of neutron reflectivity and X-ray reflectivity measurements shows an elimination of accumulated roughness for the $^{11}B_4C$ containing multilayers with a mean interface width of 4.5 Å, resulting in an increase in reflectivity at the first Bragg peak by a factor of 2.3 and 1.5 for neutron and X-ray measurements, respectively.

1. Introduction

Neutron scattering is a non-destructive analytical technique which can be a powerful tool to investigate a range of physical properties. This technique offers several interesting advantages, among others for the study of bulk materials, magnetic properties of thin films as well as the study of condensed matter. Neutron scattering however is a signal-limited technique providing relatively few neutrons to the experiment. The European Spallation Source, which is currently under construction, will be the world's most powerful neutron source [1]. Nevertheless, even the most brilliant neutron sources have a flux that is many orders of magnitudes lower than the attainable flux for e.g. X-rays at synchrotron radiation sources. Instead, the largest increase in neutron flux at the experiment is expected to come from improving the performance of neutron optical components [2].

Most key components used in neutron scattering experiments utilize so called multilayer mirrors, and Ni/Ti is the most conventional choice for neutron multilayer mirrors as the high contrast in scattering length density (SLD) provides good prospects for a high reflectance [3]. The reflectivity performance of such mirrors critically depends on the quality of the interface structure. Assuming the variation in SLD across the interface can be described by an error function, the reflectivity reduction caused by the interface width may be accounted for by introducing a Debye-Waller-like factor,

$$R = R_0 e^{-\left(2\pi m \frac{\sigma}{\Lambda}\right)^2} \tag{1}$$

where the interface width is denoted by σ, the order of the Bragg peak is indicated by m, and Λ describes the period of the multilayer. As the reduction in reflectivity is exponentially dependent on the square of the interface width, even a modest improvement in interface width can lead to a significant increase in reflectivity performance.

The current state-of-the-art neutron supermirrors that are available on an industrial scale have an average interface width of 0.7 nm, which has been characterised using simulated fits to experimental specular neutron measurements of the samples [4]. The reduction of the interface width for such multilayers has therefore been a popular area of research in the past. The interface width between the layers in a multilayer can to a great extent be attributed to a combination of nanocrystallites, formation of intermetallics, intermixing, and interdiffusion between adjacent layers in the mirror. Different attempts have been made to reduce this interface width, for example reactive magnetron sputtering of Ni layers in an Ar/air mixture has led to certain improvements for thicker layers in a supermirror, as measured using neutron reflectivity [5]. Other attempts include the addition of an ultrathin Cr layer at the Ni/Ti interfaces, to prohibit interdiffusion between the layers [6]. Another popular material for such diffusion barriers has been B_4C, which has been well-studied for EUV mirrors specially for Mo/Si multilayers in the past [7]. Our work on Cr/Sc multilayers for X-ray mirrors has shown that co-deposition of B_4C throughout the whole multilayer stack successfully amorphizes the layers getting rid of nanocrystallites at the interfaces [9].

We have investigated a novel magnetron sputter growth technique. By incorporating B_4C during deposition, it was found that the formation of nanocrystallites was inhibited, and amorphous Ni/Ti multilayers were obtained. It has however also been found that the incorporation of B_4C also limits the adatom surface mobility during growth [8]. This prevents the deposited atoms from finding energetically favourable sites at the surface, resulting in a rough surface which will deteriorate as the multilayer grows. These effects can be mitigated by applying a negative substrate bias during growth, attracting ions from the plasma to the surface giving the adatoms enough energy to migrate at the surface towards more energetically favourable positions. Such a continuous ion assistance, however, can lead to ion-induced mixing of the exposed surface of the previously deposited layer and the adatoms of the new layer that is being deposited. To overcome this issue, a modulated ion assistance scheme has been used during deposition [9]. In this scheme, an initial buffer layer is grown at a low substrate bias voltage of -30 V where the ion energy is too low to allow for surface displacement during growth, therefore creating an abrupt but rough initial layer. The remainder of the layer is then grown using a higher substrate bias voltage of -100 V where surface diffusion is possible for deposited adatoms, while the aforementioned intermixing will be limited to the initial buffer layer grown at a low substrate voltage and this remainder of the layer grown at a higher substrate voltage. Hence the energy of the ions attracted from the plasma is modulated in a way that minimize intermixing into the previous layer and then stimulates adatom mobility to create a smooth top surface before deposition of the next layer [9]. In this work, the low-neutron-absorbing isotope enriched $^{11}B_4C$ has been used to study the use of this concept in neutron multilayers, as natural B_4C is unsuitable in neutron multilayers because of the high neutron absorption of the isotope ^{10}B.

Multilayers with and without the incorporation of $^{11}B_4C$ have been investigated using a combination of Elastic Recoil Detection Analysis (ERDA) to determine the composition, and X-ray reflectivity and neutron reflectivity for structural analysis and reflectivity performance.

2. Experimental details

The samples described in this work were deposited using our ultra-high vacuum (UHV) magnetron sputtering chamber at PETRA III at the Deutsches Elektronen-Synchrotron (DESY)

in Hamburg, Germany. This deposition chamber is described in detail elsewhere [10]. The samples have been deposited on $10\times10\times0.5$ mm^3 Si (001) substrates with a native oxide that were rotated around the sample normal at a constant rate of 7 rpm during the growth process. The samples were deposited at ambient temperatures with no substrate heating. Ultra-high purity argon gas (> 99.999998%) has been used as sputtering gas at a working pressure of 3 mTorr (0.4 Pa), as measured by a capacitance manometer. The chamber was evacuated to a base pressure of $6.7\cdot10^{-6}$ Pa ($5.0\cdot10^{-8}$ Torr) using a dual turbomolecular pump setup. The sputtering targets had a constant power of 20 W and 60 W for Ni and Ti, respectively, while 35 W was used for the $^{11}B_4C$ target. For the pure sample this resulted in a deposition rate of 0.38 and 0.43 Å/s for Ni and Ti, respectively, as determined by hard X-ray reflectivity measurements of single layer films. The samples that have been co-deposited with $^{11}B_4C$ showed a deposition rate of 0.42 and 0.47 Å/s for the Ni$^{11}B_4C$ and Ti$^{11}B_4C$ layer, respectively. The applied bias on the substrate was -30 V for the initial part (0-10 Å) and -100 V for top part (10-24 Å) of each layer. Apart from the inclusion of $^{11}B_4C$, both samples have been deposited in the same system under the same conditions as described above. Both samples have a total of 104 periods, with multilayer periods of 47.0 Å and 45.8 Å for the sample with and without $^{11}B_4C$, respectively.

The samples have been measured using various characterization techniques in order to investigate the structural properties. The elemental composition of the films was determined using time-of-flight energy recoil detection analysis (ToF-ERDA) at the Tandem Laboratory at Uppsala University. A primary beam of $^{27}I^{8+}$ was used with an energy of 36 MeV at an incident angle of 67.5° relative to the surface normal, the energy detector was placed at a recoil scattering angle of 45°. A detailed description of the experimental set-up is given elsewhere [11], [12]. The measured data has been analysed using the Potku software in order to determine the atomic concentrations [13].

An analytical Tecnai G2 UT FEG microscope operating at 200 kV for a point-to-point resolution of 0.19 nm was used for transmission electron microscopy (TEM) studies. Microstructure and layer definition of Ni/Ti and Ni/Ti doped with $^{11}B_4C$ multilayers were studied using both bright field and dark field imaging as well as high resolution cross-sectional TEM. Dark field imaging was used as an approach to effectively highlight crystalline regions in the sample, while high-resolution TEM was used to investigate the layered structure in the multilayers. The cross-sectional samples were prepared using mechanical grinding and polishing followed by low-energy ion-beam milling using a Gatan precision ion polishing system.

Neutron reflectometry measurements were performed for a series of samples at Institut Laue–Langevin in Grenoble with the SuperADAM reflectometer at a monochromatic wavelength of 5.23 Å. The distance from the sample to the detector was 150 cm. Both the specular and off-specular signals were obtained simultaneously in this set-up. The pure Ni/Ti sample has been measured in a range of 0°-10° θ with a step size of 0.01°/step using a constant collection time of 50 s per step, leading to a total acquisition time of ~13.9 h. This sample has been measured using a 5 mm mask to ensure that the entire beam fits on the sample, making the alignment slightly easier. For the sample that has been co-deposited with $^{11}B_4C$, the measurement has been split up in four different regimes. The first regime was performed in a range of 0-1° θ with a step size of 0.005°/step and an acquisition time of 30 s per step. The second regime was done from 1–4° θ with a step size of 0.01°/step and a collection time of 40 s per step. The third regime was performed from 4–7° θ with a step size of 0.02°/step and a collection time of 80 s per step. The fourth and final regime was performed from 7-15° θ with a step size of 0.04/step and a collection time of 150 s per step. The total acquisition time for this sample was ~16.7 h. Footprint correction has been applied to both samples for the specular signal using the provided data reduction software at instrument site. For this correction, a trapezoidal beam was assumed after which the total data set has been normalised to the critical angle.

X-ray reflectivity measurements were performed using a Panalytical Empyrean diffractometer using a Cu X-ray tube. On the primary side, a parallel beam X-ray mirror has been used in combination with a 1/32° divergence slit, while a parallel plate collimator has been used in combination with a collimator slit at the reflected beam usingh a PIXcel-3D area detector in 0D mode. Reflectivity of the multilayers were measured in the range 0°-10° 2θ with a step size of 0.01°/step and a collection time of 0.88 s per step, giving a total measurement time of ~30 min.

In order to obtain structural parameters of the multilayer samples, simultaneous fitting of the obtained neutron and X-ray reflectivity data has been performed using the GenX fitting software, which uses the Paratt recursion formalism to simulate specular reflectivity [14]. A common challenge while obtaining structural information from such fits is to find a physical solution that describes the multilayer well while avoiding the danger of overfitting. These fits often require many fitting parameters to a dataset that does not have a unique solution, a good agreement with the experimental results does not necessarily imply that the found parameters are physically correct, in particular when these fits are done directly to material properties such as the SLD itself. Since both a reduction in SLD and an increase of interface width leads to a reduction in specular intensity for instance, it can be easy to interpret things that can not reliably be determined. For this reason, the SLD in this work has been calculated for X-rays and neutrons independently using compositional measurements obtained by ERDA.

Since X-rays interact with the electron cloud and neutrons interact with the atomic nucleus, the scattering lengths for neutrons and X-rays are completely independent from each other, providing two independent data sets that contain the same structural information. For this reason fitting to the obtained experimental data has been done simultaneously while structural parameters were coupled to each other whenever possible, giving a more reliable physical result.

3.   Results and discussion

Transmission electron microscopy (TEM) measurements were performed on both samples. Figure 1 shows the cross section for both multilayers in dark-field, bright-field, and high-resolution TEM micrographs as well as the SAED pattern for the samples. Both samples show smooth interfaces with no obvious signs of roughness accumulation. The pure Ni/Ti multilayer is clearly crystalline as can be observed in the dark-field micrographs in Figure 1 b). The SAED pattern shows a diffractive ring with diffraction spots in the growth direction corresponding to Ni nanocrystallites with [111] preferred orientation in the growth direction, consistent with other findings for such multilayers in the literature [15]. Several diffraction spots are also found that possibly can be attributed to Ni-Ti intermetallics. The $^{11}B_4C$ containing multilayer shows a single weak diffraction halo in the SAED pattern shown in Figure 1 d) which does not correspond to Ni or Ti lattices. A possible explanation is the formation of boride nanocrystallites in the sample. High resolution TEM micrographs in the dark-field (not shown) shows the sporadic presence of nano-crystallites throughout the multilayer, but the sample is predominantly amorphous as further evidenced in the dark-field TEM micrograph shown in Figure 1 e).
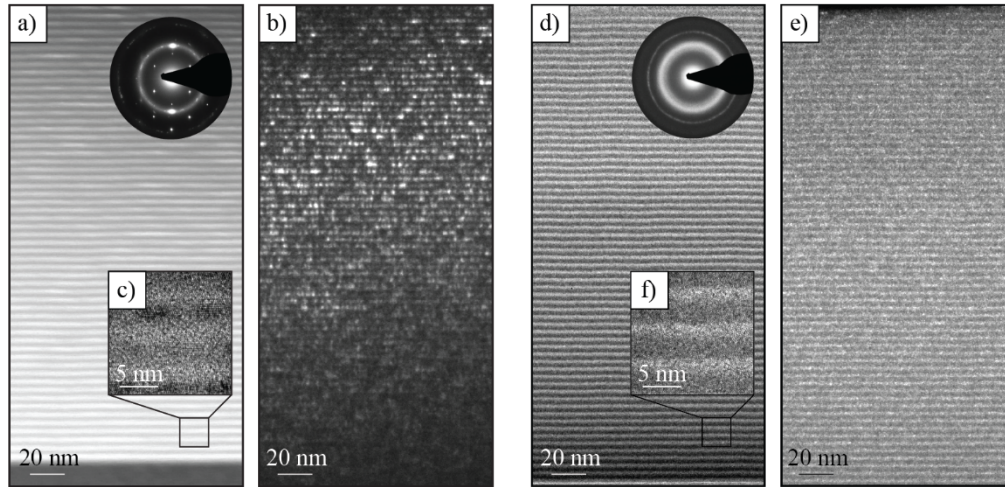
Fig. 1. a) Bright-field TEM micrograph of the pure Ni/Ti multilayer. The top right corner shows the SAED pattern of this sample. b) Dark-field TEM micrograph of the pure Ni/Ti multilayer. c) High-resolution TEM micrograph of the pure Ni/Ti multilayer d) Bright-field TEM micrograph of the $^{11}B_4C$ containing Ni/Ti multilayer. e) Dark-field TEM micrograph of the $^{11}B_4C$ containing Ni/Ti multilayer. The top right corner shows the SAED pattern of this sample. f) High-resolution TEM micrograph of the $^{11}B_4C$ containing Ni/Ti multilayer.

Compositional analysis has been performed using ERDA to obtain the elemental compositions of ^{11}B and C in the multilayers. From these measurements a clear oxide layer can be observed on the Ni/Ti multilayer grown without $^{11}B_4C$ sample, while such an oxide layer is absent from the $^{11}B_4C$ containing layer. TEM analysis also agrees with ERDA oxidation results. This shows that $^{11}B_4C$ co-deposition prevents oxidation of the multilayer, this behavior was also observed for natural B_4C in previous work [8]. The measurements show 21.9 at.% boron and 3.6 at.% carbon throughout the sample. The boron to carbon ratio present in the measured multilayers is roughly 6:1, which is somewhat higher than 4:1 as expected for an $^{11}B_4C$-target. The exact reason behind this discrepancy is uncertain. Possible explanations may be an unexpected composition in the target material or preferential resputtering of the C by the impinging Ar ions used for ion assistance. As an estimation, the total composition in each individual layer has been calculated using the deposition times for each layer from which it follows that the Ni-layer contains 19.7 and 3.2 at.% ^{11}B and C respectively, while the Ti-layer contains 24.5 at.% and 4.0 at.% ^{11}B and C, respectively. The neutron-absorbing ^{10}B isotope was not found in any of the multilayers.

Neutron reflectivity as well as X-ray reflectivity measurements were performed to investigate structural parameters of the samples. The specular signal for the multilayer that was co-deposited with $^{11}B_4C$ is compared to that of the pure Ni/Ti multilayer in Figure 2. The off-specular rocking curve at the first Bragg peak is shown in the insets of the figure. Both techniques show a significant increase in specular intensity at the first Bragg peak, from 17% to 39% and from 21% to 32% for neutron and X-ray measurements, respectively. The lower reflectivity of the higher order Bragg-peaks can be explained by the different thickness ratios within the periods as well as an observed asymmetry in interface width between both layers for the pure Ni/Ti sample, shown in Table 2 as obtained by fitting a simulated model to the experimental data. Unlike the higher order peaks, which are strongly dependent on these factors, the reflectivity at the first Bragg peak is largely unaffected by this. This makes the first order Bragg peak a better indicator for the interface width than the higher order peaks.

Both neutron and X-ray measurements show a higher specular intensity for the multilayer containing $^{11}B_4C$, despite pure Ni/Ti having a better contrast in terms of scattering length

density. This indicates a significant improvement in terms of interface width, nevertheless the ^{11}B$_4$C containing multilayer shows a clear increase in diffuse scattering as shown in the insets of Figure 2. This could indicate that the ^{11}B$_4$C containing multilayer may have more abrupt interfaces with less intermixing than the pure Ni/Ti multilayer but with a stronger vertical correlation, therefore leading to a higher off-specular intensity despite having a smaller interface width. The shoulders that can be observed at the left-hand side of the Bragg peaks in the specular signal of the pure sample indicate that several bilayers with a higher period are present in the sample. Simulations indicate however that this would not have a large impact on the overall reflectivity of the sample.
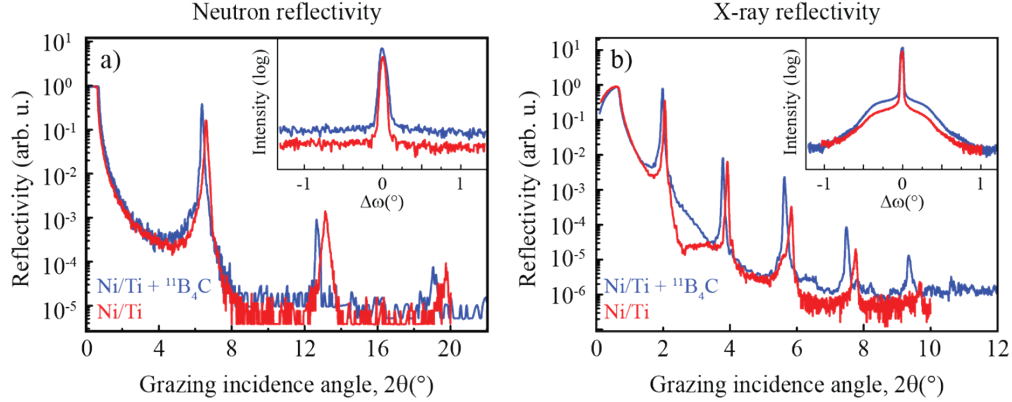
Fig. 2. a) The obtained neutron reflectivity signal for both samples. b) X-ray reflectivity data for both samples. The difference in background intensity for the X-ray reflectivity signal is due to the use of a 5 mm mask for the ^{11}B$_4$C-acontaining sample, decreasing the signal-to-noise ratio. The insets show the rocking curves for both samples at the first Bragg peak. Both rocking curves have been normalized to the peak intensity of the specular signal at the first Bragg peak.

This process has been performed for both multilayers in this study. The model assumes an independent initial interface width for each layer with a linear increase in interface width per period. This linear accumulation of interface width is set to be equal for both layers. The interface width for the Ni- and Ti containing layer in the j:th period in the multilayer is therefore determined by

$$\sigma_{Ni,j} = A \cdot j + \sigma_{Ni,initial} \text{ and } \sigma_{Ti,j} = A \cdot j + \sigma_{Ti,initial}, \tag{2}$$

where A is the increase in interface width per period, i.e. describing a roughness accumulation. The letter j indicates the period position in the stack from the substrate, and $\sigma_{Ni,initial}$ and $\sigma_{Ti,initial}$ describe the initial interface widths for the Ni- and Ti layers, respectively.

The multilayers also show a slight increase of period throughout the multilayer, which leads to a slight peak broadening, which is in particular visible at higher incidence angles. This has been incorporated into the model by allowing the layer thickness for each layer to increase linearly for each period. In order to restrict the number of fitting parameters, this increase is modelled as being equal for both layers. The thickness of each layer is therefore described as

$$d_{Ni} = D \cdot j + \Gamma \cdot \Lambda \text{ and } d_{Ti} = D \cdot j + (1 - \Gamma) \cdot \Lambda, \tag{3}$$

where D describes the increase in thickness per period, j indicates the position of the period in the stack, Γ is the ratio between the layer thicknesses defined as $\Gamma = d_{Ni}/(d_{Ni} + d_{Ti})$, and Λ is the sum of the layer thicknesses $d_{Ni} + d_{Ti}$ at the substrate. The SLD for each layer depends both on the elemental composition and on the density of the layer, and the SLD of each layer has

therefore been calculated by summing over each element in the layer using the following expression

$$SLD = \frac{\rho N_a \sum_{j=1}^{N} c_j b_j}{\sum_{j=1}^{N} c_j M_j}. \tag{4}$$

Here ρ denotes the mass density of the layer, N_a is Avogadro's number, and the elemental concentration, the scattering length and the molecular weight for each element are described by c_j, b_j and M_j, respectively. For X-rays, the scattering length b_j depends on the atomic scattering factor and therefore is wavelength dependent. For these calculations, the scattering length for X-rays has been used from tabulated values at a wavelength of 1.54 Å [16]. The compositional values are retrieved from ERDA measurements, which were used to approximate the density in each layer using the bulk densities for each element. The resulting SLD for the individual layers in each sample are given in Table 1. The structural properties of the samples were fitted within a reasonable range of the expected values given the X-ray and neutron reflectivity data. The SLD values used in this work are summarized in Table 1.

Table 1. The SLD that has been calculated for the different layers in the sample for reflectivity simulations in this work. The imaginary component of the SLD for neutrons was negligible for all layers.

Material	Neutron SLD (10^{-6} Å^{-2})	X-ray SLD (10^{-6} Å^{-2})
NiO	8.66	50.13 - 3.00i
Ni	9.42	64.46 - 1.35i
Ti	-1.91	35.53 - 2.99i
$Ni_{0.77}{}^{11}B_{0.20}C_{0.03}$	8.85	53.97 - 1.07i
$Ti_{0.71}{}^{11}B_{0.25}C_{0.04}$	-0.35	30.94 - 2.39i
SiO_2	4.19	22.72 - 0.29i
Si	2.06	19.98 - 0.46i

A limitation regarding the fitting of the X-ray data is the limited vertical coherence length of the X-ray source used for the measurements, which has found to be equal to about 116 nm. This is not enough to resolve the entire multilayer stack which has a total thickness of 490 nm, the X-ray data therefore will not show the same peak broadening that is found for neutrons. This is an issue in particular for the pure Ni/Ti sample where a clear peak broadening can be observed in the neutron data where the vertical coherence length is more than sufficient (>1 μm) to resolve the entire stack. This could not be accounted for in the fitting software that has been used. As a crude approximation, thickness accumulation as well as the starting period have therefore been determined separately for the X-ray and neutron reflectivity data in this specific sample. All other structural parameters have been coupled to both data sets.
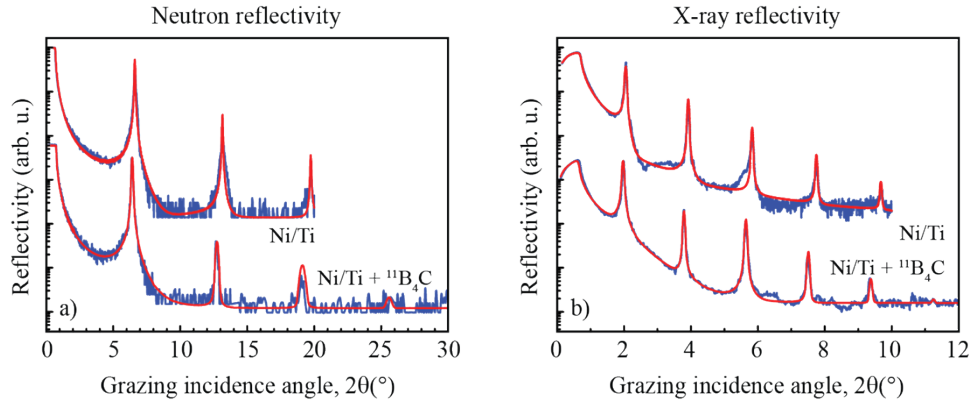
Fig. 3. a) The obtained fits to the neutron reflectivity data. b) The obtained fits to the X-ray reflectivity data. The fits were performed to both neutron and X-ray data simultaneously with coupled structural parameters.

The simulated fits to the experimental data can be observed in Figure 3. Both multilayers show an excellent agreement between the fit and the experimental data for all peaks on both data sets. The fitted structural parameters that can be extracted from these fits are found in Table 2.

Table 2. Illustration of the multilayer fitting model and obtained structural information for both multilayers. The figure of merit indicates how well the simulated model fits with the experimental data on a log-scale.

Parameter	Ni/Ti	Ni/Ti + ^{11}B$_4$C
Initial multilayer period, Λ (neutrons)	45.3 Å	47.0 Å
Initial multilayer period, Λ (X-rays)	47.7 Å	47.0 Å
Thickness accumulation per period (neutrons)	0.008 Å	0.000 Å
Thickness accumulation per period (X-rays)	0.000 Å	0.000 Å
Layer thickness ratio, Γ	0.48	0.50
Initial interface width for the Ni layer, $\sigma_{Ni,initial}$	9.6 Å	5.6 Å
Initial interface width for the Ti layer, $\sigma_{Ti,initial}$	2.9 Å	3.4 Å
Accumulated roughness	0.05 Å/period	0.00 Å/period
Ni oxide surface layer	13 Å	0 Å
Si substrate oxide	3 Å	3 Å
Figure of merit	0.13	0.10

Simulations show that given a certain material system, the average interface width of the bilayer is by far the most important structural parameter for the reflectivity at the first Bragg peak. The ratio between the interface width of the Ni and Ti layer only has a minor influence. The average interface width is therefore determined with a high degree of certainty, especially considering these fits have been performed simultaneously on neutron and X-ray reflectivity data where the structural parameters were coupled to each other. For both multilayers in this study, the overall interface width for the Ni containing layers is significantly higher than the interface width of the Ti containing layer, which is consistent with literature [7]. The mean overall interface width at the first period was found to be 6.3 Å for the pure Ni/Ti sample, with an accumulation of 0.05 Å per period. The ^{11}B$_4$C containing Ni/Ti sample was found to have a mean interface width of 4.5 Å per period without any signs of roughness accumulation as shown in Figure 4. The co-deposition of ^{11}B$_4$C in combination with the modulated ion assistance scheme does not only

significantly decrease the interface width in the multilayer, but it also prevents accumulated roughness.
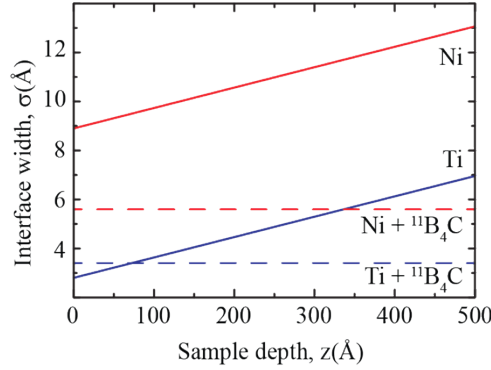

Fig. 4. The evolution of interface width for both samples according to the values found from the coupled simulated fit of neutron and x-ray reflectivity data using the parameters given in Table 2. The sample depth is measured from the substrate into the growth direction.

4. Conclusions

In this work a novel magnetron sputter growth technique where $^{11}B_4C$ co-deposition has been combined with a modulated ion assistance scheme in order to reduce interface width in Ni/Ti multilayers has been investigated. Comparison with pure Ni/Ti multilayers show a significant improvement both for neutron and X-ray reflectivity. Combined fits to experimental reflectivity data indicate an average interface width of 4.5 Å without any sign of roughness accumulation when introducing $^{11}B_4C$. This is a significant improvement from the pure Ni/Ti multilayer, which show an average initial interface width of 6.3 Å with an increase of 0.12 Å per period. The obtained interface width when using $^{11}B_4C$ offer good prospects for high-reflectivity supermirrors. Since neutron multilayers are such essential and crucial elements in any intended instrumentation, even the slightest improvement of the performance will have an immediate and large impact on all research using those instruments.

Disclosures. The authors declare no conflicts of interest.

Data Availability. Data underlying the results presented in this paper are not publicly available at this time but may be obtained from the authors upon reasonable request.

References

1. H. Danared, M. Eshraqi and M. Jensen, "The ESS Accelerator," in 57th ICFA Advanced Beam Dynamics

Workshop on High-Intensity and High-Brightness Hadron Beams (2016)

2. D. Liu, B. Khaykovich, M.V. Gubarev, J. Lee Robertson, L. Crow, B. D. Ramsey, D. E. Moncton, *Nat. Commun.*, **4**, 2556 (2013).

3. Z. Zhong, W. Zhan-Shan, Z. Jing-Tao, W. Feng-Li, W. Yong-Rong, Q. Shu-Ji and C. Ling-Yan, *Chin. Phys. Lett.*, **23**, 2678–2680 (2006).

4. T. Veres, S. Sajti, L. Cser, S. Bálint and L. Bottyán, *J. Appl. Cryst.*, **50**, 184-191 (2017).

5. M. Senthil Kumar, P. Böni and M. Horisberger, *Nucl. Instr. Meth. A*, **529**, 90-93 (2004).

6. M. Ay, C. Schanzer, M. Wolff and J. Stahn, *Nucl. Instr. Meth. A*, **562**, 389-392 (2006).

7. S. Yu. Zuyev, D.E. Pariev, R.S. Pleshkov, V.N. Polkovnikov, N.N. Salashchenko, M.V. Svechnikov, M.G. Sertsu, A. Sokolov, N.I. Chkhalo, and F. Schäfers, *J. Surf. Investig.* **13**, 169–172 (2019).

8. N. Ghafoor, F. Eriksson, A. Aquila, E. Gullikson, G. Greczynski and J. Birch, *Opt. Expr.*, **25**, 18274-18287 (2017).

9. F. Eriksson, N. Ghafoor, S. Broekhuijsen, D. Ostach, G. Greczynski, N. Schell and J. Birch, *Material Optics Express*, submitted for publication (2022).

10. J. L. Schroeder, W. Thomson, B. Howard, N. Schell, L.-Å. Näslund, L. Rogström, M. P. Johansson-Jõesaar, N. Ghafoor, M. Odén, E. Nothnagel, A. Shepard, J. Greer and J. Birch, *Rev. Sci. Instr.*, **86**, 095113 (2015).

11. H. J. Whitlow, G. Possnert and C. S. Petersson, *Nucl. Instr. Meth. B*, **27**, 448-457 (1987).

12. Y. Zhang, H. J. Whitlow, T. Winzell, I. F. Bubb, T. Sajavaara, K. Arstila and J. Keinonen, *Nucl. Instr. Meth. B*, **149**, 477-489 (1999).

13. K. Arstila, J. Julin, M. Laitinen, J. Aalto, T. Konu, S. Kärkkäinen, S. Rahkonen, M. Raunio, J. Itkonen, J.-P. Santanen, T. Tuovinen and T. Sajavaara, *Nucl. Instr. Meth. B*, **331**, 34–41 (2014).

14. A. Glavic. and M. Bjorck. *J. Appl. Cryst.*, **55**, 1063-1071 (2022).

15. P. Villars and K. Cenzual, Eds., NiB Crystal Structure: Datasheet from `PAULING FILE Multinaries Edition – 2012" in Springer Materials, Springer-Verlag Berlin Heidelberg & Material Phases Data System (MPDS), Switzerland & National Institute for Materials Science (NIMS), Japan.

16. B. L. Henke, E. M. Gullikson, and J. C. Davis, *Atomic Data and Nuclear Data Tables*, **54**, 181-342 (1993).